DOI: 10.1002/((please add manuscript number))

Article type: Article

Gadolinium-Induced Valence Structure Engineering for Enhanced Oxygen Electrocatalysis

Meng Li,# Yu Wang,# Yang Zheng, Gengtao Fu, Dongmei Sun, Yafei Li, Yawen Tang,* and Tianyi Ma**

M. Li, Y. Wang, Y. Zheng, Prof. D. Sun, Prof. Y. Li and Prof. Y. Tang

Jiangsu Key Laboratory of New Power Batteries, Jiangsu Collaborative Innovation Center of Biomedical Functional Materials, School of Chemistry and Materials Science, Nanjing Normal University, Nanjing 210023, China.

Email: tangyawen@njnu.edu.cn (Y. Tang)

Dr. G. Fu

Materials Science and Engineering Program & Texas Materials Institute, The University of Texas at Austin, Austin, Texas 78712, United States

Email: gengtaofu@gmail.com (G. Fu)

Dr. T. Ma

Discipline of Chemistry, University of Newcastle, Callaghan, NSW 2308, Australia

E-mail: tianyi.ma@newcastle.edu.au (T. Ma)

Keywords: gadolinium, cobalt, valence structure engineering, electrocatalyst, oxygen reduction reaction

Abstract: Rare earth doped materials with unique electronic ground state configuration are considered as a kind of emerging alternatives to conventional Pt/C for the oxygen reduction reaction (ORR). Herein, we for the first time investigate the gadolinium (Gd)-induced valence structure engineering for the enhanced oxygen electrocatalysis. The Gd_2O_3-Co heterostructure loaded on N-doped graphene (Gd_2O_3-Co/NG) is constructed as the target catalyst via a facile sol-gel assisted strategy. This synthetic strategy allows Gd_2O_3-Co nanoparticles to distribute uniformly on N-graphene surface and form intimate Gd_2O_3/Co interface sites. Upon the introduction of Gd_2O_3, the ORR activity of Gd_2O_3-Co/NG is significantly increased compared with Co/NG, where the half-wave potential ($E_{1/2}$) of Gd_2O_3-Co/NG is 100 mV more positive than that of Co/NG and even close to commercial Pt/C. The density functional theory (DFT) calculation and spectroscopic analysis demonstrate that, owing to intrinsic charge redistribution at the engineered interface of Gd_2O_3/Co, the coupled Gd_2O_3-Co can break the OOH*-OH* scaling relation and result in a good balance of OOH* and OH* bindings on Gd_2O_3-Co surface, and thus an enhanced ORR activity. For practical application, a rechargeable Zn–air battery employing Gd_2O_3-Co/NG as an air-cathode achieves a large power density and excellent charge-discharge cycle stability. This work provides valuable insights into the design and fabrication of novel platinum-group-metals-free highly active ORR electrocatalysts in alkaline media.

1. Introduction

With the mounting influence of energy crisis and environmental pollution, it is urgent to design a series of new energy materials and technology which are sustainable and renewable.[1-3] Exploring non-noble metal catalysts with desired activity and stability replace costly Pt-based ones for the oxygen reduction reaction (ORR) has been a significant challenge,[4, 5] for the large-scale commercialization of energy-related devices, such as rechargeable metal-air batteries[6-9] and fuel cells.[10, 11] Transition metals and their derivatives, including alloys,[12, 13] oxides,[14-16] chalcogenides,[17-20] phosphides,[21-23] carbides[24-26] and nitrides[27-29] have attracted researcher's widely attention because of their intrinsic electrochemical properties and low price. Although the fact that these alternatives were proven effectively, their electrocatalytic performances for the ORR need to be further improved in comparison to that of Pt-based catalysts, and are not satisfactory to meet the practical requirements.

Strategies to improve the ORR activity are often optimized by choosing specific support, reducing particle-size, tuning particle structure, or adding foreign promoters.[30-33] In view of the electronic interaction effect, modification of transition metal-based catalysts with foreign promoters should be a reliable strategy to regulate their electrocatalytic performance.[33-37] Recently, rare earth oxides (REO) have attracted special interest as the foreign promoters to modulate the electrocatalytic properties of various transition metals.[33, 38-42] owing to their unique electronic and chemical properties of 4f sub-

shell electrons.[43, 44] As demonstrated by Shao et al.,[39] the ORR activity of Co_3O_4/ketjenblack could be significantly improved by doping with CeO_2 REO. The rich oxygen vacancies of CeO_2 and swift transition between Ce^{3+} and Ce^{4+} would be conducive to facilitate O_2 adsorption.[40] Tang et al., also reported that CeO_2 provided a synergistic effect to improve the ORR performance of MnO_x.[41] More recently, Shanmugamthe et al. unveiled that CeO_2 coupled with metallic Co made more oxygen molecules were reduced on Co surface.[42] It is worth mentioning that most of reported REO-incorporated electrocatalysts are focused on the CeO_2-doping, and their researches are not growing as fast as expected. Since there is no unpaired electron in the tetravalent Ce, the electron conductivity of CeO_2 is relatively poor. Unlike the $4f^15d^16s^2$ electronic configuration of Ce atom, rare earth element Gd has a unique configuration $4f^75d^16s^2$ of the valence electrons in the ground state. The $4f^7$ shell in Gd has a stable semi-filled electronic structure, which theoretically make Gd_2O_3 possess good electron conductivity. It is further worth emphasizing that Gd_2O_3 has chemical characteristics similar to other oxides of the lanthanide and actinide series used as the promoters in electrocatalysis.[45] Given considerably less expensive than other commonly used noble metal catalysts, the Gd_2O_3 should have great potential to be an ideal promoter materials in electrocatalysis.

Pursuing this line of reasoning, we develop a simple yet effective sol-gel strategy to fabricate Gd_2O_3-Co/N-graphene (Gd_2O_3-Co/NG) hybrids as a high-performance electrocatalyst for the ORR in alkaline media. By this design strategy, Gd_2O_3-Co heterostructure with small particle-size can well

load on N-doped graphene surface and the interface sites are evident on Gd_2O_3-Co surface. The resulting electrocatalyst exhibits excellent ORR activity with a half-wave potential of 0.82 V, comparable to state-of-the-art Pt/C catalyst. The outstanding ORR performance of Gd_2O_3-Co/NG is highly correlated with the important synergy of Gd_2O_3 and metallic Co (*i.e.,* valence electronic effect and high oxygen vacancies), and unique features of N-graphene structure (*i.e.,* porosity and electron-rich N-doping). The DFT calculations corroborate that the synergistic interaction between Gd_2O_3 and metallic Co favors a good balance of OOH* and OH* bindings on the Gd_2O_3-Co surface. Further spectroscopic measurements suggest that the intrinsic charge redistribution at the engineered interface of Gd_2O_3/Co may induces above good balance of OOH* and OH* bindings on the Gd_2O_3/Co interface. Employed as an air-cathode in Zn–air batteries, Gd_2O_3-Co/NG hybrids exhibit a larger power density with more stable cycle life.

2. Results and Discussion

2.1 Synthesis and Characterization

The synthesis procedure of Gd_2O_3-Co/NG hybrids was illustrated briefly in Figure 1a. The synthesis began with a facile sol–gel polymerization of poly(vinyl alcohol) (PVA) and graphene oxide (GO) and metal precursors (M^{n+}). The sol–gel formation is ascribed to hydrogen bonding between PVA chains

and oxygen-containing groups of GO.[46] GO with a lone electron pair can also bind metal ions (M^{n+}) efficiently through coordination and electrostatic interaction,[47, 48] which allows reduced GO to effectively anchor Gd_2O_3-Co heterostructures. The freeze-drying was proved to be useful to get 3D porous carbon because that sublimation of the formed ice by freeze-drying avoids formation of a liquid/vapor interface.[49, 50] After freeze-drying and pyrolysis at 700 °C under 10% NH_3/Ar atmosphere, 3D N-doped graphene loaded Gd_2O_3-Co nanoparticles could be obtained. The detailed process was described in the Supporting Information. For comparison, Co/NG, Gd_2O_3/NG and pure NG samples were also synthesized via the similar procedure. The crystal structures of the as-prepared products were investigated by X-ray powder diffraction (XRD, Figure 1b). For Co/NG and pure NG, a broad diffraction peak corresponding to (002) plane of graphitic carbon at about 26.5° was clearly observed, indicating the successful reduction of GO after pyrolysis. Except a broad (002) peak for carbon, another diffraction peak of Co/NG is indexed to metallic Co phase (JCPDS Card No. 15-0806). For Gd_2O_3/NG, the diffraction peaks located at 28.6°, 33.1°, 47.5° and 56.4° can be well indexed to (222), (400), (440) and (622) reflections of cubic Gd_2O_3 phase (JCPDS Card No. 12-0797). In the case of Gd_2O_3-Co/NG, two sets of diffraction peaks associated with Gd_2O_3 and Co could be observed, which demonstrates the coexistence of Gd_2O_3 and Co phases. Compared to that of Gd_2O_3/NG, the small positive peak shift of Gd_2O_3 phase in Gd_2O_3-Co/NG may be ascribed to the interaction of Gd_2O_3 with Co metal.[42] Owing to overlapping from Gd_2O_3, the broad diffraction peak of graphitic carbon was not

obviously detected in both Gd_2O_3/NG and Gd_2O_3-Co/NG. The cubic structure of Gd_2O_3 belongs to the *Ia*−3 space group, in which Gd is six-coordinated to O (Figure S1), forming corner- and edge-sharing distorted polyhedra. Such structure may endow Gd_2O_3 with a specific number of oxygen vacancies, which results from the presence of anion vacancies, compensated by oxygen vacancies. To probe abundant oxygen vacancies of Gd_2O_3-Co/NG, the electron spin resonance (ESR) spectra were carried out (Figure 1c). Relative to Co/NG, Gd_2O_3-Co/NG and Gd_2O_3/NG exhibit the significantly increased ESR intensities at the position of g = 2.003, demonstrating the appearance of oxygen vacancies in Gd_2O_3-Co/NG after the introduction of Gd_2O_3.

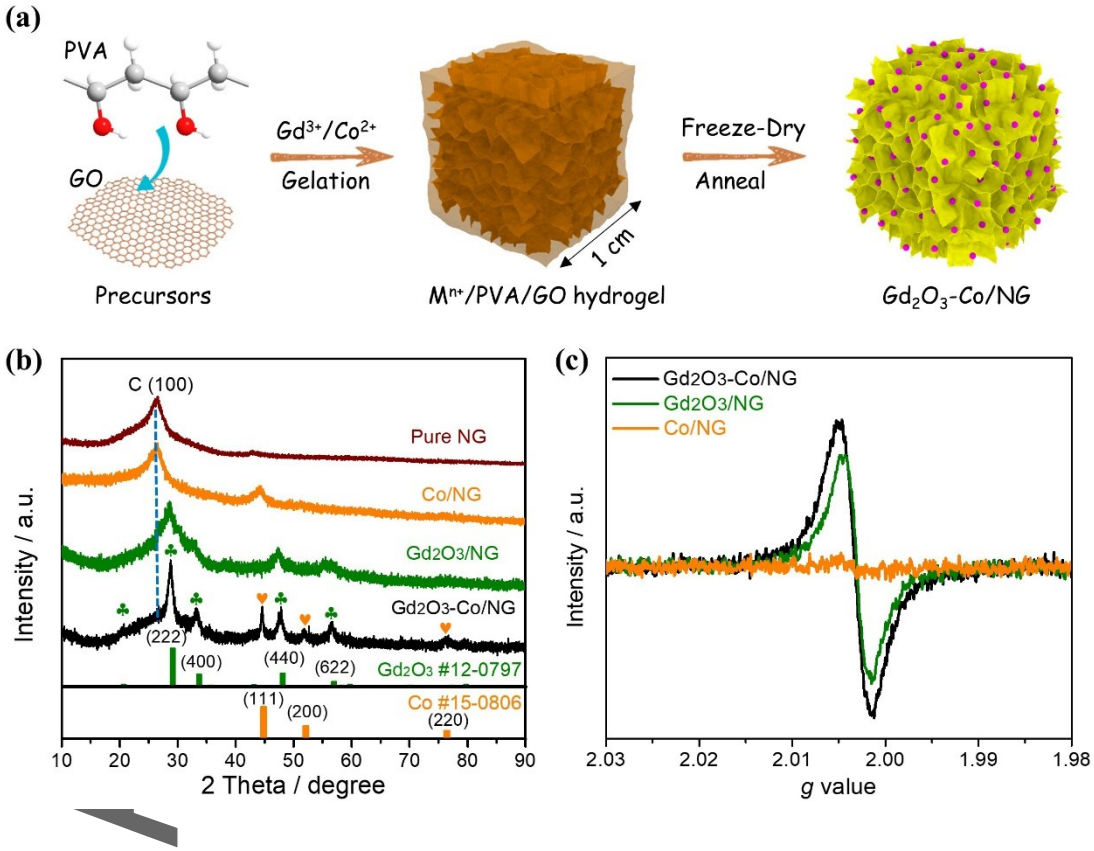

Figure 1. (a) Schematic illustration of the preparation of Gd_2O_3-Co/NG; (b) XRD patterns of Gd_2O_3-Co/NG, Co/NG, Gd_2O_3/NG and pure NG samples; (c) ESR spectra of Gd_2O_3-Co/NG, Gd_2O_3/NG and Co/NG samples.

The Gd_2O_3-Co/NG presents a 3D porous network structure composed by the crosslinked plicate nanosheets (Figure 2a-2b), as certified by scanning and transmission electron microscopy (SEM and TEM) images. N_2 adsorption–desorption isotherms (Figure 2c) reveal the typical IV-type characteristic and H_3-type hysteresis loop, indicating the existence of mesopores in Gd_2O_3-Co/NG. Because of unique 3D network, Gd_2O_3-Co/NG displays a high Brunauer–Emmett–Teller (BET) specific surface area of around 177.1 $m^2\ g^{-1}$. The 3D porous architecture together with high specific surface area would expose more accessible active-sites and facilitate the electron/mass transfer capability in electrocatalysis.[51, 52] Magnified SEM image (Figure 2d) and TEM image (Figure 2e) reflect the uniform distribution of Gd_2O_3-Co nanoparticles are well dispersed on the NG nanosheets without obvious aggregation. The statistical analysis recorded from Figure 2e indicates a narrow size-distribution and a small average particle-size of 11.2 nm (Figure 2f). 3D porous network would be effective in confining the grain growth and agglomeration of nanoparticles. Large-area energy-dispersive X-ray spectroscopy (EDX) elemental mappings (Figure 2g) proved that the uniform distribution of Gd, Co and N elements throughout the NG support. According to thermogravimetric analysis (TGA) (Figure S2), the NG-support content of Gd_2O_3-Co/NG was calculated to be about

51.1%. The atomic ratio of Gd/Co in Gd_2O_3-Co/NG determined by EDX was 54.7: 45.3 (Figure S3), which is consistent with the stoichiometric ratio of Gd and Co. To confirm the existence of the interface between Gd_2O_3 and Co species, the aberration-corrected (AC) high-angle annular dark field scanning TEM (HAADF-STEM) measurement was carried out. As shown in Figure 2h and Figure 2i, the clear interface sites between Gd_2O_3 and Co species were observed. The interplanar spacings of about 0.312 nm correspond to the (222) plane of cubic Gd_2O_3; while the interplanar spacing of about 0.210 nm is indexed to (111) plane of cubic Co. In addition, the EDX line scanning profiles and element mappings of Gd_2O_3-Co nanoparticle recorded from Figure 2i indicate that Gd_2O_3 and Co phases are located in a different geometric region of nanoparticle (Figure 2j-2l). AC HAADF-STEM results confirm that the Gd_2O_3-Co is a heterostructure. The intimate contact between Gd_2O_3 and Co phases would promise excellent synergistic effect toward catalytic reaction.

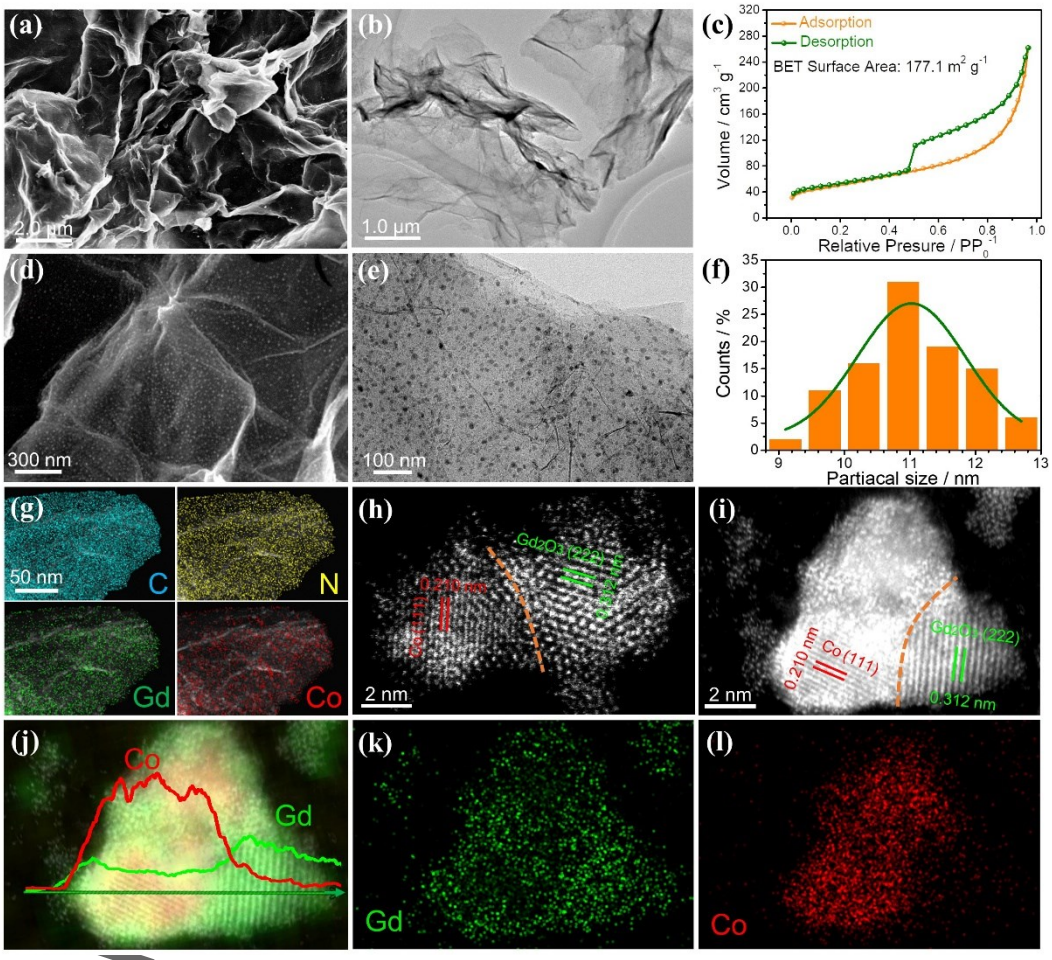

Figure 2. Large-area (a) SEM and (b) TEM images of Gd_2O_3-Co/NG; (c) N_2 adsorption–desorption isotherms; (d) Magnified SEM and (e) TEM images; and (f) particle-size distribution histogram recorded from panel (e); (g) Large-area EDX element mappings; (h and i) AC HAADF-STEM images of Gd_2O_3-Co heterostructure; (j, k and l) EDX line scanning profiles and element mappings.

The surface chemical properties of Gd_2O_3-Co/NG were further studied by X-ray photoelectron spectroscopy (XPS) in detail. XPS survey scan spectrum (Figure S4) indicates the co-presence of C, N, O, Gd and Co elements in the resulting Gd_2O_3-Co/NG. The high-resolution Co 2p XPS spectrum

(Figure 3a) displays both main peaks at 780.0 and 795.2 eV, together with associated shake-up satellites, indicating the presence of Co^{3+} species; while the peaks at 781.6 and 796.8 eV are attributed to Co^{2+}.[53] The appearance of Co^{3+}/Co^{2+} species may be ascribed to the surface oxidation of Gd_2O_3-Co/NG upon exposure to air. The existence of Gd_2O_3 was confirmed by Gd 4d XPS spectrum. As indicated by the Gd 4d spectrum (Figure 3b), the typical Gd $4d_{5/2}$ and Gd $4d_{3/2}$ orbits of Gd^{3+} state at 142.1 eV and 146.9 eV were observed clearly.[54] The Gd 4d photoemission arises from multiplet splitting of the 4d hole with $4f^7$ valence electrons to form 9D and 7D final ionic state. The O 1s spectrum presented in Figure 3c can be deconvoluted into three peaks, corresponding to oxygen atoms bounded to metals (529.6 eV), hydroxyl groups or surface adsorbed oxygen (531.1 eV) and oxygen vacancies (531.8 eV).[35] Figure 3d shows the C 1s spectrum of Gd_2O_3-Co/NG. The peak corresponding to C-N bond was observed at ~286 eV, manifesting the successful N-doping in NG. The chemical states of N1s were studied in detail via the high-resolution N 1s spectrum (Figure 3e). The spectrum could be fitted with three different N species, which correspond to pyridinic-N (398.1 eV), pyrrolic-N (400.0 eV) and graphitic-N (401.6 eV),[55, 56] respectively. Considering the size difference between N and C atoms, the introduction of N may cause the structure change of carbon materials, such as more structural defects.[57] Raman spectroscopy was performed to elucidate the structural characteristics of NG-based aerogels, including Gd_2O_3-Co/NG, Gd_2O_3/NG, Co/NG and NG samples. The detailed characterizations of Gd_2O_3/NG (Figure S5), Co/NG (Figure S6) and NG (Figure

S7) are presented in Supporting Information. The intensity ratio (I_D/I_G) of D-band and G-band offers information on the size of sp^2 domains, which suggests the degree of disorder. As viewed in Figure 3f, the I_D/I_G value of Gd_2O_3-Co/NG is estimated to be about 1.08, which is better than that of Gd_2O_3/NG (I_D/I_G= 0.98), Co/NG (I_D/I_G= 0.91), NG (I_D/I_G= 0.91) and N-free rGO (I_D/I_G= 0.80). The high I_D/I_G ratio of Gd_2O_3-Co/NG can be attributed to the distortion of carbon structure and the defects induced by N-doping and the insertion of Gd_2O_3 and Co nanoparticles.[58, 59] The high structural defects generally can endow carbons with more active-sites towards ORR and enhance the chemical adsorption of oxygen on the catalyst surface.[60, 61]

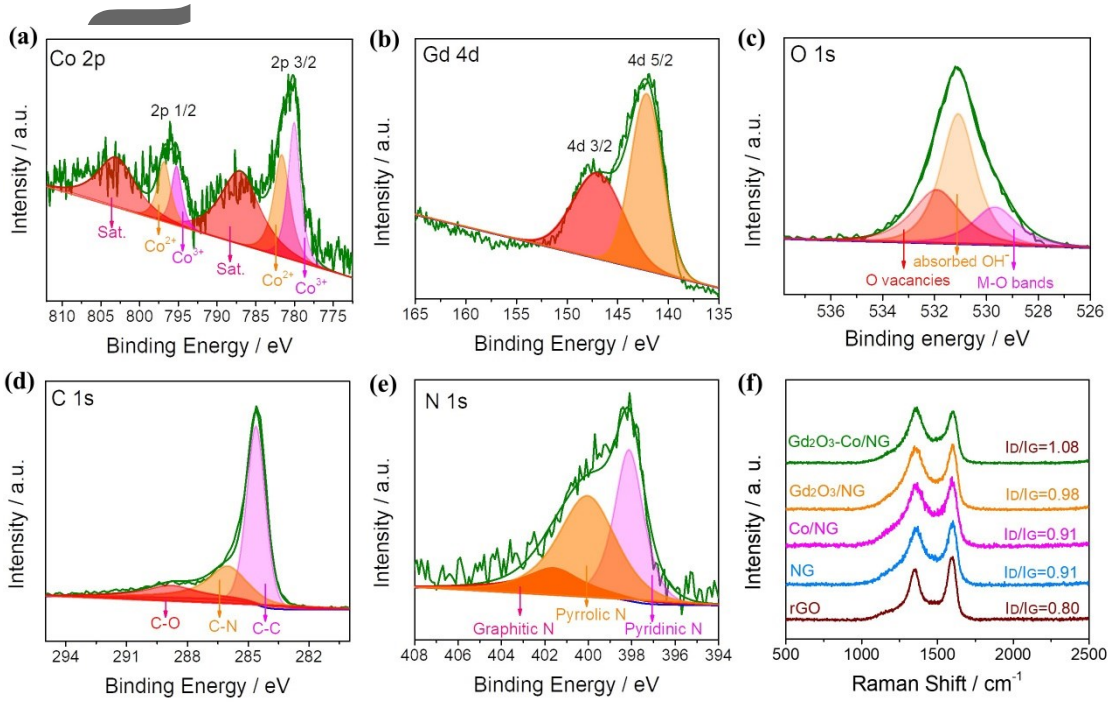

Figure 3. High-resolution XPS spectra of (a) Co 2p, (b) Gd 4d, (c) O 1s; (d) C 1s and (e) N 1s region, respectively; (f) Raman spectra of Gd_2O_3-Co/NG, Gd_2O_3/NG, Co/NG, pure NG and rGO.

2.2 Electrocatalytic Performance

The electrocatalytic performance of Gd_2O_3-Co/NG towards ORR was evaluated on the rotating disk electrode (RDE) in O_2-saturated 0.1 M KOH solution, in comparison with that of Co/NG, Gd_2O_3/NG and commercial Pt/C catalysts. The linear sweep voltammetry (LSV) curves for different catalysts are shown in Figure 4a. The Gd_2O_3-Co/NG exhibits a high electrocatalytic activity for the ORR, as judged by positive onset potential (E_{onset}= 0.93 V) and half-wave potentials ($E_{1/2}$= 0.82 V). The half-wave potential of Gd_2O_3-Co/NG is very close to that of Pt/C catalyst, highlighting the excellent ORR activity of Gd_2O_3-Co/NG. The E_{onset} and $E_{1/2}$ values of Gd_2O_3-Co/NG significantly outperform those of Co/NG (E_{onset}= 0.82 V, $E_{1/2}$= 0.69V) and Gd_2O_3/NG (E_{onset}= 0.78 V, $E_{1/2}$= 0.58 V), indicating the important synergistic effects between Gd_2O_3 and Co. After the introduction of Gd_2O_3-Co to pure NG, the ORR activity of Gd_2O_3-Co/NG was greatly improved (Figure S8), suggesting that the coupling of Gd_2O_3-Co with NG is also critical to excellent ORR activity. The Gd_2O_3-Co/NG is also among the most active transition-metal based electrocatalysts for the ORR (Table S1). To get insight into ORR reaction kinetics, the Tafel slopes were calculated from the polarization curves. As shown in Figure 4b, Gd_2O_3-Co/NG has a lower Tafel slope (59 mV dec^{-1}) than that of Co/NG (62 mV dec^{-1}) and Gd_2O_3/NG (90 mV dec^{-1}), which even is comparable to that of Pt/C (60 mV dec^{-1}), suggesting the favorable reaction kinetics and fast electron transport on Gd_2O_3-Co/NG electrode. To quantitatively

understand the ORR process of Gd_2O_3-Co/NG, the current-potential curves were performed at different rotation (Figure 4c). The electron transfer number (n) was calculated to be about 4.0 at 0.4–0.6 V based on the Koutecky-Levich plots (inset in Figure 4c), indicating the 4-electron dominated transfer pathway during the ORR process. The ring current profiles associated with reduction of peroxide species (H_2O_2) formed during ORR were presented in the upper panel of Figure S9, from which the H_2O_2 yield from Gd_2O_3-Co/NG was determined to be < 15% and the electron transfer number was estimated to be > 3.70 (Figure 4d). These values are better than those of Co/NG and Gd_2O_3/NG samples, and even close to those of Pt/C catalyst. These results demonstrate the highly selective 4-electron pathway catalyzed by Gd_2O_3-Co/NG. The stability of Gd_2O_3-Co/NG was determined by chronoamperometry in O_2-saturated 0.1 M KOH solution. The Gd_2O_3-Co/NG offers better electrochemical stability than that of Pt/C and other two catalysts, with < 5% decay in ORR activity over 40000 s of continuous operation at half-wave potential (Figure 4e). Taken together, Gd_2O_3-Co/NG is demonstrated to be a highly-active and stable electrocatalyst for the ORR. The outstanding ORR performance can be mainly ascribed to the synergistic effects of Gd_2O_3, Co and 3D porous NG structure. The high-density interfaces in Gd_2O_3-Co heterostructures and 3D porous network in N-doped graphene provide a rich variety of active-sites and a large electrochemical active area (ECSA), as well as short ion-diffusion pathway during the ORR.[62] The ECSA of catalysts can reflected by the electrochemical double layer capacitance (C_{dl}), as it is linearly proportional to the

ECSA. It is found that the C_{dl} value of Gd_2O_3-Co/NG (21.5 mF cm^{-2}) is much higher that of Co/NG (12.9 mF cm^{-2}) and Gd_2O_3/NG (5.1 mF cm^{-2}) counterparts (Figure S10 and Figure 4f), demonstrating the significantly improved ECSA after the incorporation of Gd_2O_3 and Co species. Furthermore, 3D porous network structure can also prevent the nanoparticles from agglomerating and dissolving during the reaction, thus resulting in good electrochemical stability. After the chronoamperometry test, the 3D porous structure of Gd_2O_3-Co/NG were well preserved and Gd_2O_3-Co nanoparticles were well dispersed on the NG surface (Figure S11). XRD pattern in Figure S12 shows that two sets of diffraction peaks associated with Gd_2O_3 and Co were still preserved; While the signals of Gd 3d and Co 2p XPS spectra for recovered Gd_2O_3-Co/NG sample did not change significantly compared with initial Gd_2O_3-Co/NG sample (Figure S13).

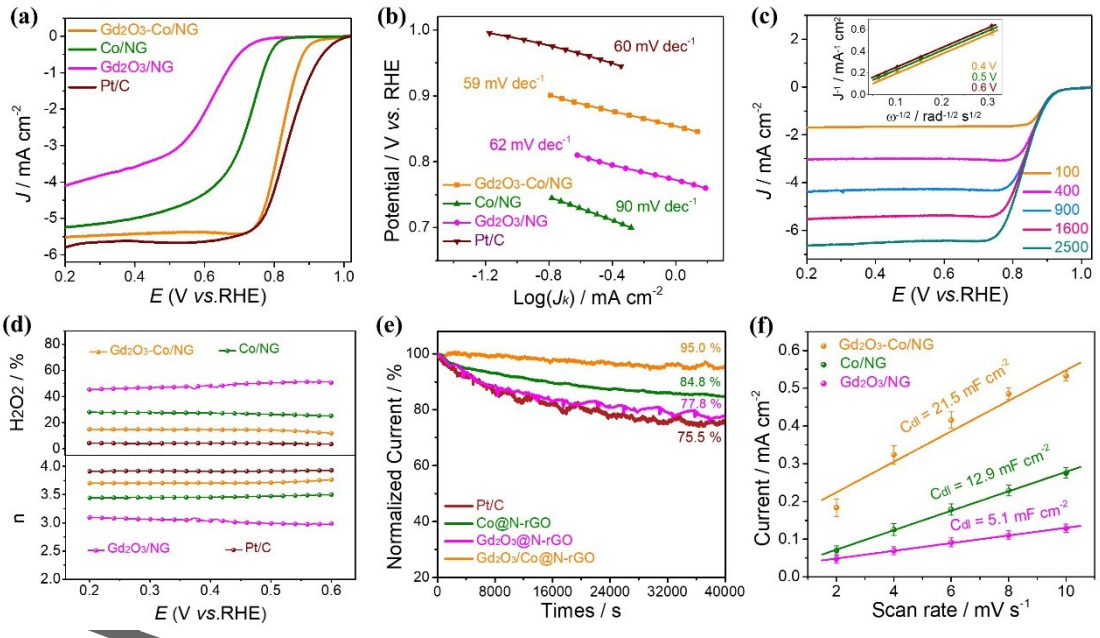

Figure 4. (a) LSV curves of four catalysts in O_2-saturated 0.1 M KOH (rotation rate: 1600 rpm; sweep rate: 5 mV s^{-1}); (b) Tafel plots derived from panel (a); (c) LSV curves of Gd_2O_3-Co/NG at various rotation rates, the inset shows the Koutecky–Levich plots at different potentials; (d) H_2O_2 production yields and electrons transfer number (n); (e) Chronoamperometric responses at half-wave potential in O_2-saturated 0.1 M KOH (percentage of current retained vs operation time); (f) The linear fitting of scan rate with capacitive current density.

2.3 Mechanism Investigation

To identify the possible ORR activity origin, we performed spin-polarized density functional theory plus Hubbard-U (DFT+U) computations to explore the ORR process over the as-prepared Gd_2O_3-Co/NG with focus on the roles of Gd and Co (see Experimental Section for computational details). As the ORR activity of a given catalyst is typically governed by its adsorption free energies of reaction intermediates,[63] including OOH* (ΔG_{OOH^*}), O* (ΔG_{O^*}) and OH* (ΔG_{OH^*}), we first studied the interactions between Gd_2O_3 slab and these intermediates. The geometry structures of intermediates on the Gd_2O_3 slab are plotted in Figure 5a. Our calculations shown that ΔG_{OOH^*}, ΔG_{O^*} and ΔG_{OH^*} of Gd_2O_3 are about 3.56, 2.39 and 0.31 eV; the energy difference between of ΔG_{OOH^*} and ΔG_{OH^*} ($\Delta G_{OOH^*} - \Delta G_{OH^*}$) is 3.25 eV, in accordance with the well-established linear scaling relation of $\Delta G_{OOH^*} - \Delta G_{OH^*}$ = ~3.2 eV.[63, 64] It remains somewhat difficult to effectively modulate ORR activity owing to the existence of robust scaling relation, i.e., the balance between OOH* formation and OH* removal.[63]

Accordingly, the relatively low activity of Gd_2O_3 can be seen from its ΔG_{OH^*}, which is much smaller than that of Pt (111) plane (0.79 eV)[65] and the optimal value (0.86 eV).[64] The unfavorable ΔG_{OH^*} of Gd_2O_3 (quite strong OOH* adsorption) also revealed that its potential-limiting step is OH* removal, as shown in the free energy diagram of reaction process (Figure 5c). The geometry structures of intermediates on Gd_2O_3-Co slab are plotted in Figure 5b. It was found that all the intermediates adsorptions become weaker after involving Co into Gd_2O_3 slab. For example, the ΔG_{OH^*} of Gd_2O_3-Co has been considerably increased from 0.31 to 1.51 eV, indicating that OH* removal can be easily achieved on Gd_2O_3-Co and is no longer the potential-limiting step. The ΔG_{OOH^*} and ΔG_{O^*} of Gd_2O_3-Co were found to be 4.25 and 3.18 eV, respectively. Intriguingly, the synergy of Gd_2O_3 and Co broke the OOH*-OH* scaling relation ($\Delta G_{OOH^*} - \Delta G_{OH^*}$ = 2.74 eV for Gd_2O_3-Co), demonstrating that the enhancement on OH* may not much sacrifice the favorable OOH* binding. As expected, the theoretical activity of Gd_2O_3-Co was increased by ~0.36 V compared to sole Gd_2O_3, in good agreement with our experimental finding, although the ORR over Gd_2O_3-Co is now limited by OOH* formation step because of its slightly weak OOH* adsorption (Figure 5d). The breaking of scaling relation may be attributed to the different configurations of OH* and OOH* on Gd_2O_3-Co, where the former is the end-on adsorption on Co site and the latter is the side-on type with a co-binding over both Gd and Co sites. The oxidized Co site intrinsically prefers a weak intermediate binding, while the

support of Gd site can enhance intermediate binding, consequently reaching a good balance of OOH* and OH* bindings on the Gd_2O_3-Co surface.

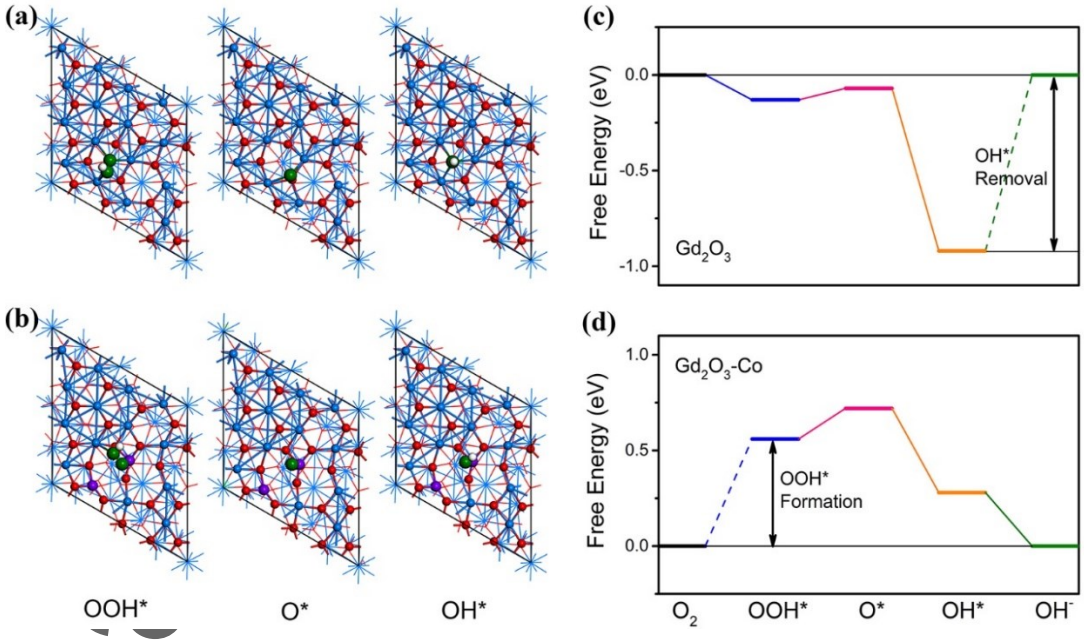

Figure 5. Views of intermediates OOH*, O*, and OH* on (a) Gd_2O_3 and (b) Gd_2O_3-Co. Azure, red, violet and white balls denote Gd, O, Co and H atoms, respectively. The O atoms of intermediates is highlighted by blue balls. Free energy diagrams of ORR path over (c) Gd_2O_3 and (d) Gd_2O_3-Co at the theoretical equilibrium potential (U = 1.23 V *vs* RHE). The dash lines and arrows represent potential-limiting step.

The good balance of OOH* and OH* bindings on the Gd_2O_3-Co surface may be caused by the intrinsic charge redistribution at the engineered interface of Gd_2O_3/Co, because the oxygen adsorption at the initial step is closely related to the electron transfer.[66] This speculation can be

supported by the previous reported CeO_x/M (M=Pt and Co etc.) studies.[42, 67, 68] For example, DFT calculations by Kim et al., demonstrated that CeO_2 can perturbe the electronic structure of Co species and further optimize the binding energy of intermediate oxygenated adsorbates.[69] In view of the different work functions of Gd_2O_3 and Co, the flow of electrons would occur through the metal/semiconductor interface;[70] while Gd_2O_3 as one of important REO may regulate the electronic structure of Co because the 4f orbital of Gd is available for electron sharing and bonding.[71] Unlike CeO_x/M catalysts, however, the $4f^7$ shell in Gd has a stable semi-filled electronic structure, which theoretically make Gd_2O_3 possess better electron conductivity than CeO_2. To elucidate the change of electronic structure of Gd_2O_3 and Co species, the XPS spectra were further performed (Figure 6). Compared with Co/NG sample, the binding energy of Co 2p in Gd_2O_3-Co/NG has a positive shift of about 0.4 eV (Figure 6a), indicating that the Gd_2O_3 has an electronic interaction with Co species. This result was further verified by the shift in the Gd 4d spectrum of the Gd_2O_3-Co/NG towards a lower binding energy relative to that in Gd_2O_3/NG (Figure 6b). Such charge redistribution at the engineered interface of Gd_2O_3/Co can lead to the fast charge-transfer capacity of Gd_2O_3-Co/NG electrode, which was verified by electrochemical impedance spectroscopy (EIS). As depicted in Figure 6c, the Nyquist plots for Gd_2O_3-Co/NG display a smaller charge-transfer resistance (61 Ω) than that of Co/NG (84 Ω) and Gd_2O_3/NG (173 Ω) counterparts. On the other hand, the charge redistribution occurred between Gd_2O_3 and Co at the interface can induce abundant oxygen vacancies, as confirmed by above ESR

spectra (Figure 1c), which also increases the oxygen absorbance on the Gd_2O_3-Co surface,[72] consequently facilitating the activation and partial dissociation of O_2. After the ORR test, the ESR intensity of recovered sample also remains at a high concentration (Figure 6d), indicating the high stability of oxygen vacancies in Gd_2O_3-Co/NG.

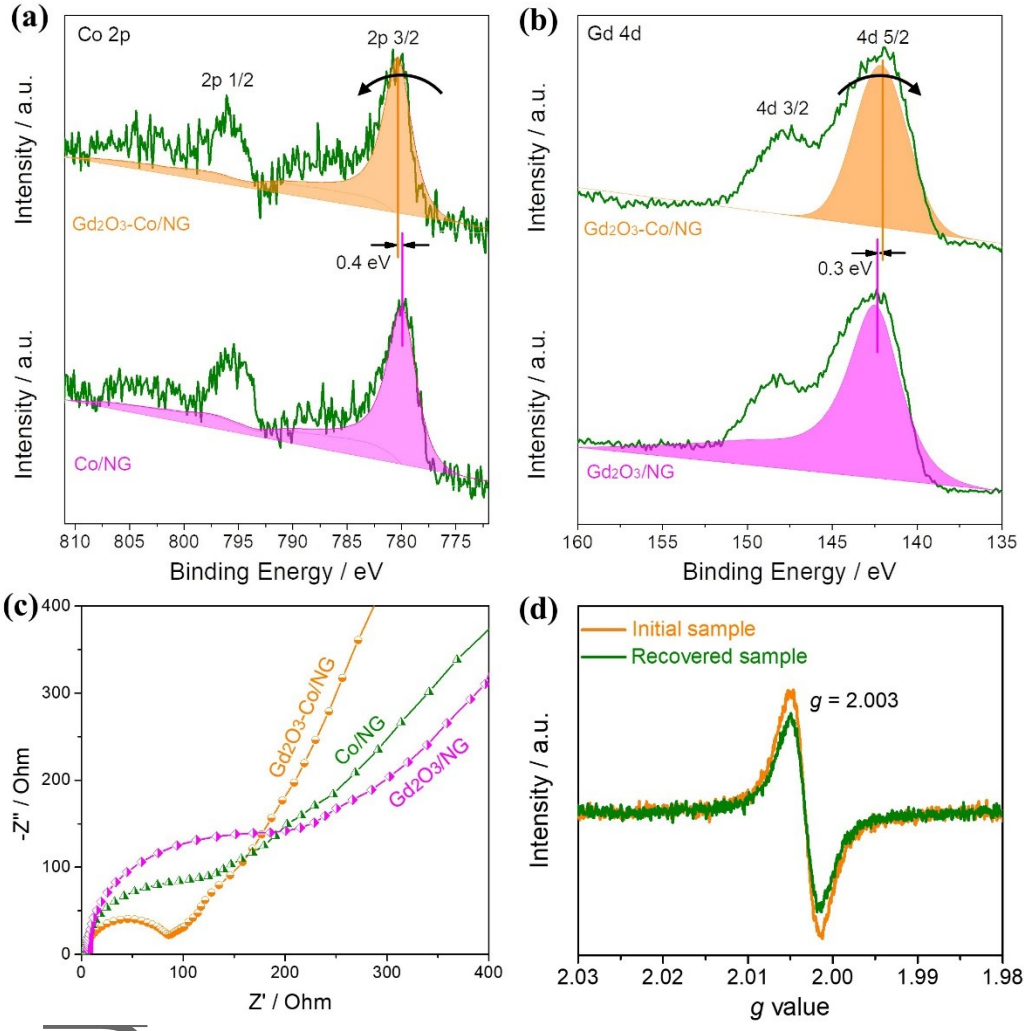

Figure 6. (a) Co 2p XPS spectra of the Gd_2O_3-Co/NG and Co/NG; (b) Gd 4d XPS spectra of the Gd_2O_3-Co/NG and Gd_2O_3/NG; (c) EIS Nyquist plots of catalysts at the open circuit potential; (c) ESR spectra of initial and recovered Gd_2O_3-Co/NG samples.

2.4 Practical Zn-Air Batteries

Apart from outstanding ORR activity, the Gd_2O_3-Co/NG can deliver a low overpotential of about 376 mV at 10 mA cm^{-2} towards oxygen evolution reaction(OER), which is very close to art-of-the-state RuO_2 catalyst (353 mV), and better than that of Co/NG, Gd_2O_3/NG and NG catalysts (Figure S14). Because of the bifunctional property of Gd_2O_3-Co/NG, a home-made Zn-air battery (Figure S15) was further built to evaluate the actual feasibility of Gd_2O_3-Co/NG. The carbon paper supported Gd_2O_3-Co/NG worked as the air-cathode, a 0.3 mm Zn plate as the anode and 0.2 M $ZnCl_2$ + 6.0 M KOH solution as the electrolyte (Figure 7a). As the reference, the Zn-air battery with Pt/C+RuO_2 as the air-cathode was also tested. The discharge polarization curves and the power density curves were presented in Figure 7b. As observed, the Gd_2O_3-Co/NG-based battery exhibits a larger peak power density (114.3 mW cm^{-2}) than that of Pt/C+RuO_2-based battery (103.1 mW cm^{-2}), which is also comparable to or larger than that of the most active Co-based bifunctional electrocatalysts reported to date (Table S2). The Gd_2O_3-Co/NG can enable the Zn–air battery with a specific capacity of 734.6 mA h g_{Zn}^{-1} at 5 mA cm^{-2} (Figure 7c), corresponding to a high energy density of 892.7 Wh kg_{Zn}^{-1}. These values outperform the battery with Pt/C+RuO_2 air-cathode (specific capacity of 692.6 mA h g_{Zn}^{-1} and energy density of 834.6 Wh kg_{Zn}^{-1}). Considering large power density and energy density, a red light-emitting diode (LED) screen can be powered by three cells in series with Gd_2O_3-Co/NG as air-cathode

(Figure 7d), suggesting its promising application in Zn–air batteries. Moreover, the Gd_2O_3-Co/NG-based battery shows the better cycle stability than that of Pt/C+RuO_2-based battery, as indicated in Figure 7e. The charge voltage of Gd_2O_3-Co/NG-based battery was well maintained after the continuous 160 cycles while the RuO_2+Pt/C-based battery showed a poor cycle life. These results indicate that the Gd_2O_3-Co/NG air-cathode has attractive potential in the Zn–air batteries.

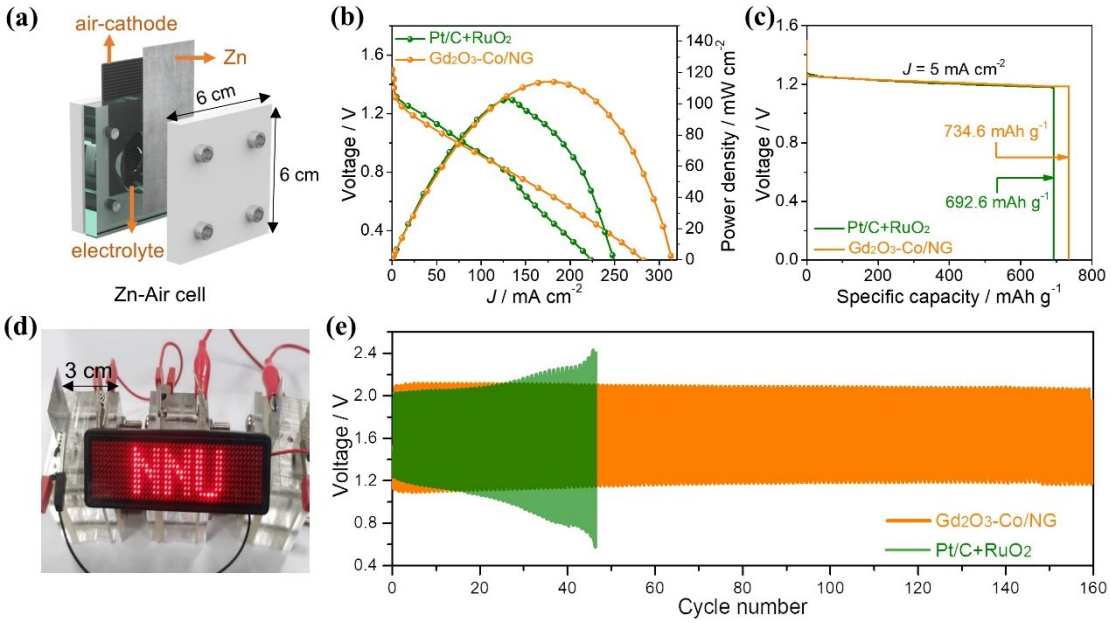

Figure 7. (a) Schematic illustration of Zn-air battery configuration; (b) The discharge polarization curves and the corresponding power density curves of Gd_2O_3-Co/NG and Pt/C+RuO_2 based batteries; (c) Discharge curves at a constant current density of 5 mA cm^{-2}; (d) LEDs powered by three Zn–air batteries in series with Gd_2O_3-Co/NG as the air-cathode; (e) The galvanostatic charge–discharge curves of Zn-air batteries.

3. Conclusion

In summary, we prepared a novel N-graphene supported Gd_2O_3-Co heterostructures (Gd_2O_3-Co/NG) by a facile sol-gel assisted strategy, and demonstrate that the incorporation of Gd_2O_3 into metallic Co can dramatically enhance its electrocatalytic performance for the oxygen reduction reaction (ORR). The introduction of high-valent Gd_2O_3 into Co is found to make the charge redistribution at the engineered interface of Gd_2O_3/Co, creating more oxygen vacancies and optimizing surface electronic structure of catalyst. Thus, the resulting efficient charge-transfer ability and more active sites exposed on Gd_2O_3/Co interface endow Gd_2O_3-Co/NG with outstanding electrocatalytic activity and stability for the ORR. Moreover, the results of DFT calculation agree well with the experimental observation where a better balance of OOH* and OH* bindings on the Gd_2O_3-Co surface is demonstrated. As an air-cathode in Zn-air batteries, the Gd_2O_3-Co/NG exhibits a large power density (114.3 mW cm^{-2}), a high energy density (892.7 Wh kg_{Zn}^{-1}) and an excellent cyclability (over 160 cycles at 10 mA cm^{-2}). We believe the current work would make a significant impact in the development of rare earth doped materials for energy storage and conversion.

Supporting Information

Supporting Information is available from the Wiley Online Library or from the author.

Acknowledgements

M. Li and Y. Wang contributed equally to this work. This work was financially supported by National Natural Science Foundation of China (21875112, 21873050 and 21576139), Australian Research Council (ARC) through Discovery Early Career Researcher Award (DE150101306) and Linkage Project (LP160100927), Faculty of Science Strategic Investment Funding 2019 of University of Newcastle, and CSIRO Newcastle Energy Centre. The authors are also grateful for the supports from National and Local Joint Engineering Research Center of Biomedical Functional Materials and a project sponsored by the Priority Academic Program Development of Jiangsu Higher Education Institutions.

Received: ((will be filled in by the editorial staff))

Revised: ((will be filled in by the editorial staff))

Published online: ((will be filled in by the editorial staff))

References

1. Liu, X.; Dai, L., *Nat. Rev. Mater.* **2016,** *1*, 16064.

2. Chu, S.; Cui, Y.; Liu, N., *Nat. Mater.* **2017,** *16*, 16.

3. Cano, Z. P.; Banham, D.; Ye, S.; Hintennach, A.; Lu, J.; Fowler, M.; Chen, Z., *Nat. Energy* **2018,** *3*, 279-289.

4. Shui, J.; Wang, M.; Du, F.; Dai, L., *Sci. Adv.* **2015,** *1*, e1400129.

5. Xue, L.; Li, Y.; Liu, X.; Liu, Q.; Shang, J.; Duan, H.; Dai, L.; Shui, J., *Nat. Commun.* **2018,** *9*, 3819.

6. Bian, J.; Su, R.; Yao, Y.; Wang, J.; Zhou, J.; Li, F.; Wang, Z. L.; Sun, C., *ACS Appl. Energy Mater.* **2019,** *2*, 923-931.

7. Liu, G.; Li, J.; Fu, J.; Jiang, G.; Lui, G.; Luo, D.; Deng, Y.-P.; Zhang, J.; Cano, Z. P.; Yu, A.; Su, D.; Bai, Z.; Yang, L.; Chen, Z., *Adv. Mater.* **2019,** *31*, 1806761.

8. Han, X.; Ling, X.; Wang, Y.; Ma, T.; Zhong, C.; Hu, W.; Deng, Y., *Angew. Chem. Int. Ed.* **2019,** *58*, 5359-5364.

9. Yang, D.; Zhang, L.; Yan, X.; Yao, X., *Small Methods* **2017,** *1*, 1700209.

10. Long, Z.; Li, Y.; Deng, G.; Liu, C.; Ge, J.; Ma, S.; Xing, W., *Anal. Chem.* **2017,** *89*, 6309-6313.

11. Wu, R.; Song, Y.; Huang, X.; Chen, S.; Ibraheem, S.; Deng, J.; Li, J.; Qi, X.; Wei, Z., *J. Power Sources* **2018,** *401*, 287-295.

12. Su, C. Y.; Cheng, H.; Li, W.; Liu, Z. Q.; Li, N.; Hou, Z.; Bai, F. Q.; Zhang, H. X.; Ma, T. Y., *Adv. Energy Mater.* **2017,** *7*, 1602420.

13. Fu, Y.; Yu, H.-Y.; Jiang, C.; Zhang, T.-H.; Zhan, R.; Li, X.; Li, J.-F.; Tian, J.-H.; Yang, R., *Adv. Funct. Mater.* **2018,** *28*, 1705094.

14. Zhou, T.; Xu, W.; Zhang, N.; Du, Z.; Zhong, C.; Yan, W.; Ju, H.; Chu, W.; Jiang, H.; Wu, C.; Xie, Y., *Adv. Mater.* **2019,** *31*, 1807468.

15. Li, Y.; Zhong, C.; Liu, J.; Zeng, X.; Qu, S.; Han, X.; Deng, Y.; Hu, W.; Lu, J., *Adv. Mater.* **2017,** *30*, 1703657.

16. Tan, P.; Chen, B.; Xu, H.; Cai, W.; He, W.; Ni, M., *Appl. Catal. B: Environ.* **2019,** *241*, 104-112.

17. Han, X.; Zhang, W.; Ma, X.; Zhong, C.; Zhao, N.; Hu, W.; Deng, Y., *Adv. Mater.* **2019,** *31*, 1808281.

18. Ma, Z.; Dou, S.; Shen, A.; Tao, L.; Dai, L.; Wang, S., *Angew. Chem. Int. Ed.* **2015,** *54*, 1888-1892.

19. Jang, J.-H.; Lee, E.; Xiao, P.; Park, K.; Kim, I. Y.; Henkelman, G.; Hwang, S.-J.; Kwon, Y.-U.; Goodenough, J. B., *Adv. Energy Mater.* **2018,** *8*, 1702037.

20. Zeng, Z.; Fu, G.; Yang, H. B.; Yan, Y.; Chen, J.; Yu, Z.; Gao, J.; Gan, L. Y.; Liu, B.; Chen, P., *ACS Mater. Lett.* **2019,** *1*, 432-439.

21. Qin, Q.; Jang, H.; Chen, L.; Nam, G.; Liu, X.; Cho, J., *Adv. Energy Mater.* **2018,** *8*, 1801478.

22. Ahn, S. H.; Manthiram, A., *Small* **2017,** *13*, 1702068.

23. Chen, J.; Fan, C.; Hu, X.; Wang, C.; Huang, Z.; Fu, G.; Lee, J.-M.; Tang, Y., *Small* **2019,** *15*, 1901518.

24. Cui, Z.; Li, Y.; Fu, G.; Li, X.; Goodenough, J. B., *Adv. Mater.* **2017,** *29*, 1702385.

25. Xiao, M.; Zhu, J.; Feng, L.; Liu, C.; Xing, W., *Adv. Mater.* **2015,** *27*, 2521-2527.

26. Yang, W.; Liu, X.; Yue, X.; Jia, J.; Guo, S., *J. Am. Chem. Soc.* **2015,** *137*, 1436-1439.

27. Wu, M.; Zhang, G.; Qiao, J.; Chen, N.; Chen, W.; Sun, S., *Nano Energy* **2019,** *61*, 86-95.

28. Vaughn Ii, D. D.; Araujo, J.; Meduri, P.; Callejas, J. F.; Hickner, M. A.; Schaak, R. E., *Chem. Mater.* **2014,** *26*, 6226-6232.

29. Fu, G.; Cui, Z.; Chen, Y.; Xu, L.; Tang, Y.; Goodenough, J. B., *Nano Energy* **2017,** *39*, 77–85.

30. Wang, Y.-J.; Zhao, N.; Fang, B.; Li, H.; Bi, X. T.; Wang, H., *Chem. Rev.* **2015,** *115*, 3433-3467.

31. Yang, S.; Tak, Y. J.; Kim, J.; Soon, A.; Lee, H., *ACS Catal.* **2017,** *7*, 1301-1307.

32. Guo, S.; Zhang, S.; Sun, S., *Angew. Chem. Int. Ed.* **2013,** *52*, 8526-8544.

33. Gao, W.; Wen, D.; Ho, J. C.; Qu, Y., *Mater. Today Chem.* **2019,** *12*, 266-281.

34. Tao, L.; Shi, Y.; Huang, Y.-C.; Chen, R.; Zhang, Y.; Huo, J.; Zou, Y.; Yu, G.; Luo, J.; Dong, C.-L.; Wang, S., *Nano Energy* **2018,** *53*, 604-612.

35. Liu, Y.; Ma, C.; Zhang, Q.; Wang, W.; Pan, P.; Gu, L.; Xu, D.; Bao, J.; Dai, Z., *Adv. Mater.* **2019,** *31*, 1900062.

36. Yang, Y.; Wang, Y.; Xiong, Y.; Huang, X.; Shen, L.; Huang, R.; Wang, H.; Pastore, J. P.; Yu, S. H.; Xiao, L.; Brock, J. D.; Zhuang, L.; Abruna, H. D., *J. Am. Chem. Soc.* **2019,** *141*, 1463-1466.

37. Wang, Y.; Zou, Y.; Tao, L.; Wang, Y.; Huang, G.; Du, S.; Wang, S., *Nano Res.* **2019**.

38. Wei, H.; Su, X.; Liu, J.; Tian, J.; Wang, Z.; Sun, K.; Rui, Z.; Yang, W.; Zou, Z., *Electrochem. Commun.* **2018,** *88*, 19-23.

39. Liu, K.; Huang, X.; Wang, H.; Li, F.; Tang, Y.; Li, J.; Shao, M., *ACS Appl. Mater. Interfaces* **2016,** *8*, 34422-34430.

40. Xia, W.; Li, J.; Wang, T.; Song, L.; Guo, H.; Gong, H.; Jiang, C.; Gao, B.; He, J., *Chem. Commun.* **2018,** *54*, 1623-1626.

41. Chen, J.; Zhou, N.; Wang, H.; Peng, Z.; Li, H.; Tang, Y.; Liu, K., *Chem. Commun.* **2015,** *51*, 10123-10126.

42. Sivanantham, A.; Ganesan, P.; Shanmugam, S., *Appl. Catal. B: Environ.* **2018,** *237*, 1148-1159.

43. Majeed, S.; Shivashankar, S. A., *J. Mater. Chem. B* **2014,** *2*, 5585.

44. Yu, Y.; Wang, X.; Gao, W.; Li, P.; Yan, W.; Wu, S.; Cui, Q.; Song, W.; Ding, K., *J. Mater. Chem. A* **2017,** *5*, 6656-6663.

45. Huber, G. W.; Butala, S. J.; Lee, M. L.; Bartholomew, C. H., *Catal. Lett.* **2001,** *74*, 45-48.

46. Bai, H.; Li, C.; Wang, X.; Shi, G., *Chem. Commun.* **2010,** *46*, 2376-2378.

47. Sitko, R.; Turek, E.; Zawisza, B.; Malicka, E.; Talik, E.; Heimann, J.; Gagor, A.; Feist, B.; Wrzalik, R., *Dalton Transactions* **2013,** *42*, 5682-5689.

48. Fu, G.; Yan, X.; Chen, Y.; Xu, L.; Sun, D.; Lee, J.-M.; Tang, Y., *Adv. Mater.* **2018,** *30*, 1704609.

49. Job, N.; Théry, A.; Pirard, R.; Marien, J.; Kocon, L.; Rouzaud, J.-N.; Béguin, F.; Pirard, J.-P., *Carbon* **2005,** *43*, 2481-2494.

50. Tamon, H.; Ishizaka, H.; Yamamoto, T.; Suzuki, T., *Carbon* **1999,** *37*, 2049-2055.

51. Fu, G.; Wang, Y.; Tang, Y.; Zhou, K.; Goodenough, J. B.; Lee, J.-M., *ACS Mater. Lett.* **2019,** *1*, 123-131.

52. Hu, X.; Chen, Y.; Zhang, M.; Fu, G.; Sun, D.; Lee, J.-M.; Tang, Y., *Carbon* **2019,** *144*, 557-566.

53. Wan, W.; Liu, X.; Li, H.; Peng, X.; Xi, D.; Luo, J., *Appl. Catal. B: Environ.* **2019,** *240*, 193-200.

54. Lv, X.; Wang, X.; Li, T.; Wei, C.; Tang, Y.; Yang, T.; Wang, Q.; Yang, X.; Chen, H.; Shen, J.; Yang, H.; Ke, H., *Small* **2018**, e1802904.

55. Li, J.; Xia, W.; Tang, J.; Tan, H.; Wang, J.; Kaneti, Y. V.; Bando, Y.; Wang, T.; He, J.; Yamauchi, Y., *Nanoscale Horiz.* **2019**, 4, 1006-1013.

56. Wang, D.; Xiao, L.; Yang, P.; Xu, Z.; Lu, X.; Du, L.; Levin, O.; Ge, L.; Pan, X.; Zhang, J.; An, M., *J. Mater. Chem. A* **2019**, **7**, 11007-11015.

57. Singh, S. K.; Takeyasu, K.; Nakamura, J., *Adv. Mater.* **2019,** *31*, 1804297.

58. Zhang, J.; Zhang, C.; Zhao, Y.; Amiinu, I. S.; Zhou, H.; Liu, X.; Tang, Y.; Mu, S., *Appl. Catal. B: Environ.* **2017,** *211*, 148-156.

59. Jiang, H.; Liu, Y.; Li, W.; Li, J., *Small* **2018,** *14*, 1703739.

60. Yan, D.; Li, Y.; Huo, J.; Chen, R.; Dai, L.; Wang, S., *Adv. Mater.* **2017,** *29*, 1606459.

61. Zhu, J.; Li, W.; Li, S.; Zhang, J.; Zhou, H.; Zhang, C.; Zhang, J.; Mu, S., *Small* **2018,** *14*, 1800563.

62. Guan, C.; Sumboja, A.; Zang, W.; Qian, Y.; Zhang, H.; Liu, X.; Liu, Z.; Zhao, D.; Pennycook, S. J.; Wang, J., *Energy Stor. Mater.* **2019,** *16*, 243-250.

63. Kulkarni, A.; Siahrostami, S.; Patel, A.; Nørskov, J. K., *Chem. Rev.* **2018,** *118*, 2302-2312.

64. Viswanathan, V.; Hansen, H. A.; Rossmeisl, J.; Nørskov, J. K., *ACS Catal.* **2012,** *2*, 1654-1660.

65. Tripković, V.; Skulason, E.; Siahrostami, S.; Nørskov, J. K.; Rossmeisl, J., *Electrochim. Acta* **2010,** *55*, 7975-7981.

66. Nørskov, J. K.; Rossmeisl, J.; Logadottir, A.; Lindqvist, L.; Kitchin, J. R.; Bligaard, T.; Jonsson, H., *J. Phys. Chem. B* **2004,** *108*, 17886-17892.

67. Masuda, T.; Fukumitsu, H.; Fugane, K.; Togasaki, H.; Matsumura, D.; Tamura, K.; Nishihata, Y.; Yoshikawa, H.; Kobayashi, K.; Mori, T.; Uosaki, K., *J. Phys. Chem. C* **2012,** *116*, 10098-10102.

68. Lv, L.; Zha, D.; Ruan, Y.; Li, Z.; Ao, X.; Zheng, J.; Jiang, J.; Chen, H. M.; Chiang, W.-H.; Chen, J., *ACS nano* **2018,** *12*, 3042-3051.

69. Kim, J.-H.; Shin, K.; Kawashima, K.; Youn, D. H.; Lin, J.; Hong, T. E.; Liu, Y.; Wygant, B. R.; Wang, J.; Henkelman, G.; Mullins, C. B., *ACS Catal.* **2018,** *8*, 4257-4265.

70. Xue, Z. H.; Su, H.; Yu, Q. Y.; Zhang, B.; Wang, H. H.; Li, X. H.; Chen, J. S., *Adv. Energy Mater.* **2017,** *7*, 1602355.

71. He, X.; Yi, X.; Yin, F.; Chen, B.; Li, G.; Yin, H., *J. Mater. Chem. A* **2019,** *7*, 6753-6765.

72. Jin, W.; Chen, J.; Liu, B.; Hu, J.; Wu, Z.; Cai, W.; Fu, G., *Small* **2019,** *15*, 1904210.

The table of contents entry: This work for the first time investigates the gadolinium (Gd)-induced valence structure engineering for the enhanced oxygen electrocatalysis. Experimental and theoretical results demonstrate the synergy of Gd_2O_3 and Co can break the OOH*-OH* scaling relation owing to intrinsic charge redistribution at the engineered interface of Gd_2O_3/Co, resulting in a good balance of OOH* and OH* bindings on the surface of Gd_2O_3-Co. The Gd_2O_3-Co/NG air-cathode delivers large power density and high energy density, as well as excellent cycle life in rechargeable Zn–air batteries.

Keywords: gadolinium, cobalt, valence structure engineering, electrocatalyst, oxygen reduction reaction

Authors: Meng Li,# Yu Wang,# Yang Zheng, Gengtao Fu,* Dongmei Sun, Yafei Li, Yawen Tang,* and Tianyi Ma*

Title: Gadolinium-Induced Valence Structure Engineering for Enhanced Oxygen Electrocatalysis

TOC figure